Integral field spectroscopy of two radio galaxies at $z \sim 2.3^{\star}$

S. F. Sánchez[1] and A. Humphrey[2]

[1] Centro Astronómico Hispano Alemán, Calar Alto, (CSIC-MPG), C/Jesús Durbán Remón 2-2, 04004 Almeria, Spain
e-mail: sanchez@caha.es
[2] Korea Astronomy and Space Science Institute, 61-1 Hwaam-dong, Yuseong-gu, Daejeon 305-348, Republic of Korea

ABSTRACT

Aims. In this article we study the morphology, kinematics and ionization properties of the giant ionized gas nebulae surrounding two high redshift radio galaxies, 4C 40.36 ($z = 2.27$) and 4C 48.48 ($z = 2.34$).
Methods. Integral field spectroscopy observations were taken using the PPAK bundle of the PMAS spectrograph, mounted on the 3.5 m on the Calar Alto Observatory, in order to cover a field-of-view of $64'' \times 72''$ centered in each radio galaxy. The observations spanned 5 nights, using two different spectral resolutions (with *FWHM* ~ 4 Å and ~ 8 Å respectively), covering the optical wavelength range from ~ 3700 Å to ~ 7100 Å, which corresponds to the rest-frame ultraviolet range from ~ 1100 Å to ~ 2000 Å. Various emission lines are detected within this wavelength range, including Lyα (1216 Å), NV (1240 Å), CIV (1549 Å), HeII (1640 Å), OIII] (1663 Å) and CIII] (1909 Å). The dataset was used to derive the spatial distribution of the flux intensity of each of these lines and the gas kinematics. The properties of the emission lines in the nuclear regions were studied in detail.
Results. In agreement with previous studies, we find that both objects are embedded in a large ionized gas nebula, where Lyα emission is extended across ~ 100 kpc or more. The CIV and HeII emission lines are also spatially extended. The nebulae are generally aligned with the radio axis, although we detect emission far from it. In 4C+48.48, there is a band of low Lyα/CIV running perpendicular to the radio axis, at the location of the active nucleus. This feature might be the observational signature of an edge-on disk of neutral gas. The kinematics of both nebulae are inconsistent with stable rotation, although they are not inconsistent with infall or outflow.

Key words. galaxies: active – galaxies: high-redshift – galaxies: quasars: emission lines

1. Introduction

High redshift radio galaxies (HzRGs) are often surrounded by giant Lyα nebulae which sometimes extend for more than 100 kpc (e.g., McCarthy et al. 1990a; Reuland et al. 2003; Villar-Martín et al. 2003, 2007a) and sometimes beyond the radio structure (e.g., Eales et al. 1993; Kurk et al. 2002; Maxfield et al. 2002). Giant Lyα nebulae have also been found associated with other classes of high-z objects, both active and non active ones, radio loud and radio quiet (e.g., Christensen et al. 2006; Steidel et al. 2001). They are frequently aligned with the radio axis (McCarthy et al. 1995), showing an irregular morphology (e.g., Reuland et al. 2003).

In the rest-frame ultraviolet (UV) wavelength range, the giant nebulae associated with HzRGs show a variety of strong emission lines, with Lyα usually being the brightest, followed by CIVλ1550, HeIIλ1640 and CIII]λ1909 (hereafter CIV, HeII and CIII]). A multitude of weaker lines have also been detected in deep spectra (e.g. Vernet et al. 2001). Based on comparisons between emission line ratios and various ionization models, the line emitting gas is substantially enriched with metals, and is ionized predominantly by the hard radiation field of the active nucleus (e.g., Vernet et al. 2001; Humphrey et al. 2008). In a few extreme cases, however, young stars or shocks may also make a significant contribution to the ionization of this gas (e.g. Villar-Martín et al. 2007a; Maxfield et al. 2002). The nebulae

have typical masses of $\sim 10^{9-10}$ $M_{\odot}$, Lyα luminosities of the order of $\sim 10^{43-44}$ erg s^{-1} and electron densities of a few to several hundred cm^{-3} (e.g., McCarthy 1993; Reuland et al. 2003).

These nebulae often show high velocity dispersions (*FWHM* > 1000 km s^{-1}) associated with, and confined by, the radio structures (e.g., Villar-Martín et al. 2003). It is likely that these large velocity dispersions are a consequence of interactions between the radio structure and the ambient interstellar medium, which are thought to result in outflows (e.g., Villar-Martín et al. 2003; Humphrey et al. 2006; van Ojik et al. 1997).

In addition, the giant nebulae associated with HzRGs also contain gas with significantly lower velocity dispersions, which shows no clear relationship with the radio source, and in many cases is observed to extend far beyond it (i.e., ~ 500 km s^{-1}: Villar-Martín et al. 2002, 2003). These nebulae seem to be present too, although not in all the cases, in other kinds of AGNs, like radio-quiet QSOs (e.g., Christensen et al. 2006; Husemann et al. 2008). Humphrey et al. (2007a) have recently proposed that this *quiescent* gas is in infall towards the central regions of the host galaxy. The importance of this gas in feeding the AGN activity, as a reservoir of gas for galaxy assembling at high-redshift (e.g., di Matteo et al. 2005), or its role in the AGN feedback process is still unclear (e.g., Kang et al. 2007; Best 2007).

Most previous studies of the giant ionized nebulae around HzRGs have been undertaken using long-slit spectroscopy, usually with the slit aligned with the radio structure (e.g. Villar-Martín et al. 2003). A few other studies have made use of narrow band images of Lyα (e.g. Reuland et al. 2003). While both of these types of observation have resulted in a significant

Table 1. Summary of the observations.

Date	Grating	Wavelength range (Å)	*FWHM** (Å)	Sampling (Å/pix)	Object	Exposure Time (s)
31/05/05	V600	3700–5350	3.9	1.5	4C 40.36	5×1800
01/06/05	V600	3700–5350	3.9	1.5	4C 40.36	5×1800
02/06/05	V300	3700–7100	7.8	3.2	4C 40.36	4×1800
03/06/05	V600	3700–5350	3.9	1.5	4C 40.36	3×1800
04/06/05	V600	3700–5350	3.9	1.5	4C 40.36	3×1800
01/06/05	V600	3700–5350	3.9	1.5	4C 48.48	6×1800
02/06/05	V300	3700–7100	7.8	3.2	4C 48.48	5×1800
03/06/05	V600	3700–5350	3.9	1.5	4C 48.48	5×1800
04/06/05	V600	3700–5350	3.9	1.5	4C 48.48	3×1800

(*) Errors are too low to be quoted.

expansion in our understanding of the giant nebulae, they were limited by a lack of spatial information or a lack of spectral information, respectively. Integral field spectroscopy (IFS) has a clear advantage over both of these methods, in that spectral and 2-dimensional spatial information can be obtained simultaneously. For this reason, we began an observational program of IFS of powerful HzRGs at $z \sim 2-3$ using VIMOS on the VLT, and PMAS/PPAK on the 3.5 m telescope at the Calar Alto Observatory (Villar-Martín et al. 2006, 2007b). The main goal of this programme is to characterize the morphology, kinematics and ionization conditions of the extended ionized gas surrounding these objects.

In this paper, we present our results based on PPAK observations of two powerful HzRGs, 4C 40.36 ($z = 2.27$) and 4C 48.48 ($z = 2.34$). Both were selected from the 4C ultrasteep spectrum compendium (e.g. Chambers et al. 1996a, and reference therein), and are known to have spatialy extended, low surface brightness emission-line nebulae (Chambers et al. 1996b). Longslit spectroscopy for these two sources has been presented by Vernet et al. (2001) and Villar-Martín et al. (2003).

The layout of this article is as follows: in Sect. 2 we give details of the observational strategy and data reduction. In Sect. 3 we describe the analysis of the data, including the analysis of the two dimensional distribution of intensity of the different emission lines (Sect. 3.1), and the line fitting (Sect. 3.2). In Sect. 4 we present the different results from the analysis, describing the properties of the nuclear spectra (Sect. 4.1), the morphology of the emission lines (Sect. 4.2), the ionization conditions at different locations (Sect. 4.3), and the gas kinematics (Sect. 4.4). In Sect. 5 we discuss the result, and summarise the conclusions of this paper.

2. Observations and data reduction

The observations were carried out between May 31st and June 4th 2005, at the 3.5 m telescope of the Calar Alto observatory, using the Potsdam MultiAperture Spectrograph (PMAS: Roth et al. 2005) in the PPAK mode (Verheijen et al. 2004; Kelz et al. 2006). The atmospheric conditions were stable, with clear nights, but were not photometric. The seeing was variable, ranging between 0.7″ and 1.2″.

The PPAK fibre bundle consists of 382 fibres of 2.7″ diameter each (see Fig. 5 in Kelz et al. 2006). Of these, 331 fibres (the science fibres) are concentrated in a single hexagonal bundle covering a field-of-view of 72″ × 64″, with a filling factor of ∼65%. The sky is sampled by 36 additional fibres, distributed in 6 bundles of 6 fibres each, located following a circular distribution at ∼90″ away from the center and at the edges of the central

hexagon. The sky-fibres are distributed among the science ones in the pseudo-slit, in order to have a good characterization of the sky. The remaining 15 fibres are used for calibration purposes, as described below. Cross-talk between adjacent fibres is estimated as less than 5% when using a pure aperture extraction (see below). The distribution of the fibres in the pseudo-slit does not follow any regular distribution in comparison with their distribution in the focal plane of the telescope (Kelz et al. 2006), which minimizes the effect of the cross-talk. Two different gratings with different resolutions, wavelength coverage and exposure times were used. Table 1 gives a log of the observations, including the date, the grating, the wavelength range covered, the instrumental resolution (*FWHM* of the sky-emission lines), the wavelength sampling at the detector, the target, and the exposure time (number of exposures × length of individual exposures). The *FWHM* of the instrumental profile corresponds to 424 km s^{-1} for the V600 grating, and 672 km s^{-1} for the V300 grating, at the redshifted wavelength of Lyα.

Data reduction was performed using R3D (Sánchez 2006), in combination with IRAF packages (Tody 1993)[1] and E3D (Sánchez 2004). The reduction consists of the standard steps for fibre-based integral-field spectroscopy. A master bias frame was created by averaging all the bias frames observed during the night and was subtracted from the science frames.

The individual exposures from each night (see Table 1) were then combined using IRAF routines, clipping any probable cosmic rays. The location of the spectra in the CCD was determined using a continuum illuminated exposure taken before the science exposures. Each spectrum was extracted from the science frames by coadding the flux within an aperture of 5 pixels around this location along the cross-dispersion axis for each pixel in the dispersion axis, and was stored in a row-staked-spectrum file RSS (Sánchez 2004). Wavelength calibration was performed using a HeHgCd lamp exposure obtained from archive data, and corrected for distortions using ThAr exposures obtained simultaneously to the science exposures through the calibration fibres (indicated above). Differences in the fibre-to-fibre transmission throughput were corrected by comparing the wavelength-calibrated RSS science frames with the corresponding continuum illuminated ones. The sky emission was determined by using the spectra obtained throughout the sky-fibres, interpolating to recover the sky-spectrum at the location of any other fibre as described in Sánchez (2006), and it was then subtracted from the science spectra. Each night we obtained spectra
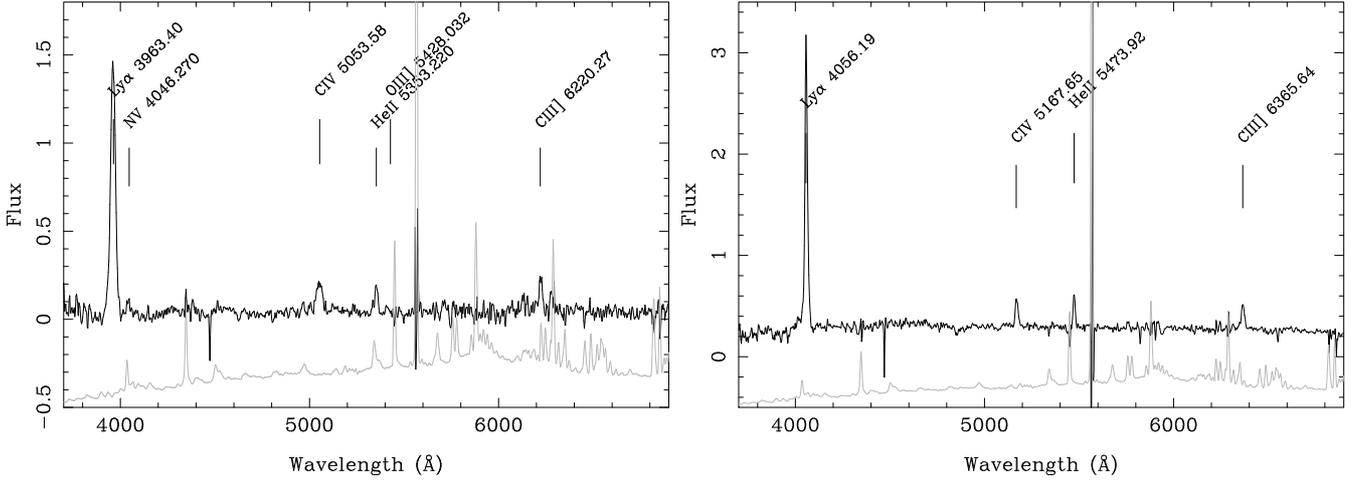

Fig. 1. Spectra extracted from the V300 IFS data for both objects, 4C 40.36 (*left panel*) and 4C 48.48 (*right panel*), corresponding to the fibre with the peak emission in Lyα in units of 10^{-16} erg s^{-1} cm^{-2} arcsec^{-2} Å^{-1} (black solid line). The identification of the detected emission lines and their observed wavelength are presented. For comparison purposes a scaled version of the night sky emission spectrum has been included in both figures (grey solid line). Strong residuals from an imperfect sky subtraction are appreciated in the spectra, in particular at $\sim$5577 Å. Some emission lines, like HeII in the case of 4C 40.36, may be affected by the imperfect subtraction of adjacent night sky emission lines.

of the spectrophotometric standard star Hz44 that we used to perform the flux calibration. The galactic extinction is low towards both objects $E(B - V) = 0.062$ and $E(B - V) = 0.089$ mag, for 4C 40.36 and 4C 48.48 respectively, and hence no correction for galactic extinction was applied to the data. Any uncertainties introduced by not applying the extinction correction are expected to be substantially smaller than those introduced by our flux calibration. The large size of the fibres and the low air-mass of the object during the observations minimize the effects of the differential atmospheric refraction. We checked its possible effect by inspecting the location of field stars across the field-of-view at each wavelength, finding no appreciable displacement. Thus, we did not perform a correction for this effect.

Once reduced, the different exposures taken on different nights were combined to produce a final frame for each grating setting. The final combined exposures times were 28 800 s for 4C 40.36 with the V600 grating and 7200 s with the V300 one, and 25 200 s for 4C 48.48 with the V600 grating and 9000 s with the V300 one. We estimate the depth of the combined exposures as follows. First, we measuring the standard deviation of the background in a wavelength region free of emission. Then, we calculate the flux of an emission line with a *FWHM* similar to the instrumental profile and an average flux per pixel of 3 times the background standard deviation. The resulting 3σ detection limit for an emission line ranges between $\sim$2–5 $\times$ 10^{-17} erg s^{-1} cm^{-2} arcsec^{-2} for the four final datacubes.

3. Data analysis

The wavelength range of our V300 data includes the redshifted Lyα (1216 Å), NV (1240 Å), CIV (1549 Å), HeII (1640 Å), OIII] (1663 Å) and CIII] (1909 Å) lines. In the case of the data using the V600 grating, only Lyα (1216 Å), NV (1240 Å) and CIV (1549 Å) fell within the spectral coverage. We extracted the spectrum of the fibre corresponding to the peak intensity of Lyα by using E3D, for each object and grating (i.e., a 2.7″ aperture spectrum). Figure 1 shows these extracted spectra for each object corresponding to the V300 grating data, together with a label for each of the previously listed emission lines detected in the spectra and their corresponding observed wavelength. Based on

these wavelengths the estimated redshifts were $z \sim 2.261$ for 4C 40.36, and $z \sim 2.336$ for 4C 48.48, similar to the objects' nominal redshifts.

3.1. Emission line images and spatial registration

Prior to performing any further analysis, the IFS data were spatially registered with astrometric calibrated images, in order to correctly place the detected structures in the sky. For this, we extract narrow-band images at the redshifted wavelength of each of the detected emission lines and the adjacent continuum, blueshifted and redshifted with respect to the emission line. The width of all the narrow-band images was fixed to 116 Å, which corresponds to the typical width of a standard narrow-band filter (*FWHM* $\sim$ 80–100 Å). We are considering wavelengths in the observer-frame. Having extracted the narrow-band images, the adjacent continua images were combined and subtracted from the emission line ones, obtaining, for each line, an emission line image free of continuum. Since the typical *FWHM* of these lines is much narrower than the selected width for the narrow-band images it is expected that the noise increases somewhat after continuum subtraction. However, using this width the obtained emission line images can be directly compared with similar published narrow-band images. On the other hand, selecting this width we ensure that all the flux from the emission lines, even the wings, are included in the narrow-band images. We checked the results creating images with narrower bands ($\sim$50 Å), and we found no significant differences. In addition a broad-band image comprising the wavelength range of our V300-grating data was extracted from the datacubes ($\sim$3700−7100 Å). This image is dominated by the continuum emission of the sources within the field-of-view (appart from the HzRGs, in which the Lyα still dominates).

To register the IFS data we first compare the Lyα emission line images with those published by Chambers et al. (1996). For 4C 40.36 they published a registered *U*-band image, which samples Lyα at the redshift of the object. The peak of the Lyα emission is coincident with that of the UV continuum emission in this object, as shown in the available Keck spectra (e.g., Villar-Martín et al. 2006; Humphrey 2005). We register the peak
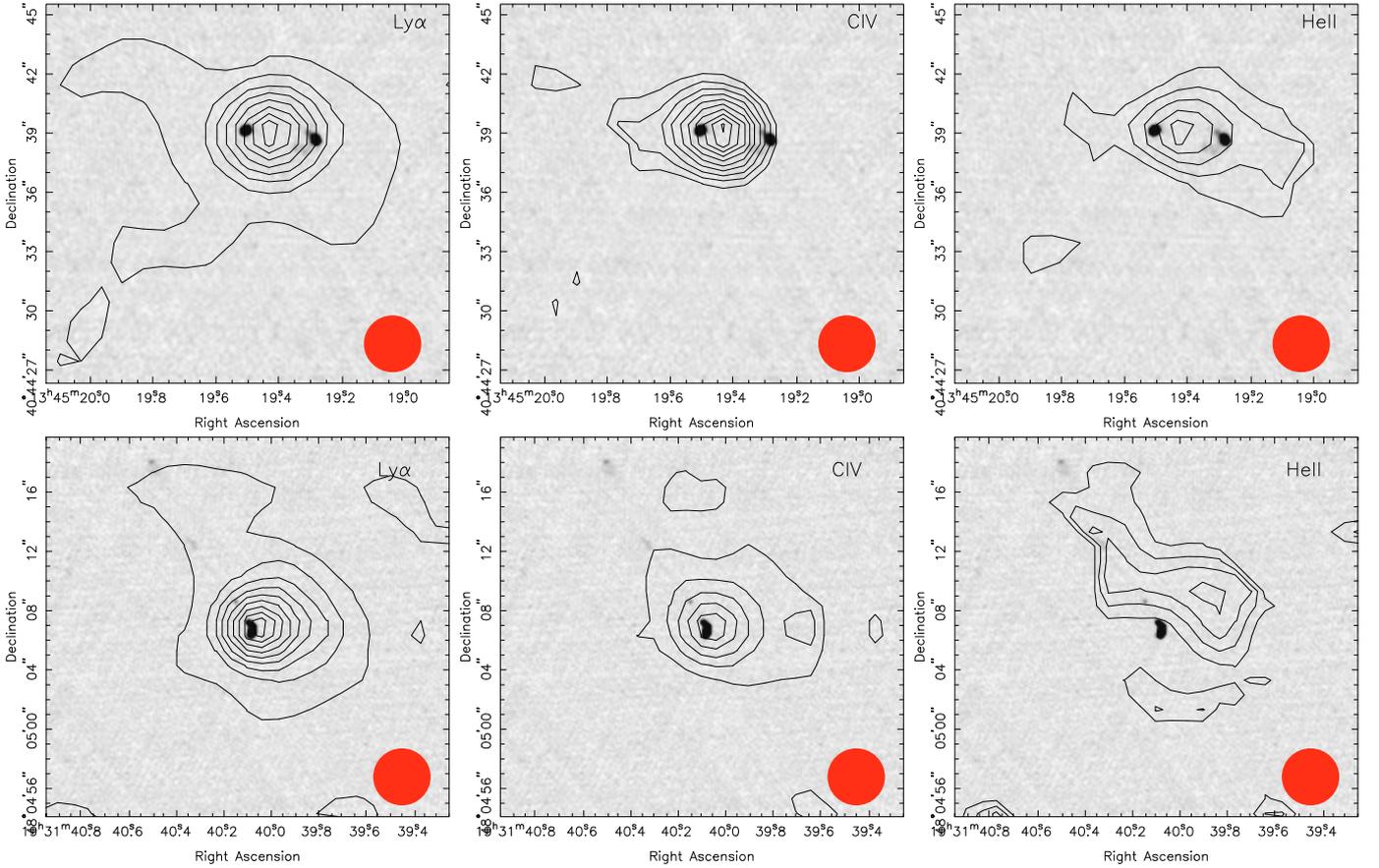
Fig. 2. *Top-left panel*: contour plot of a narrow-band image of Lyα extracted from the interpolated IFS datacube of the radio galaxy 4C 40.36, together with a grayscale image of the radio map at 5 GHz, obtained at the VLA with A configuration (Carilli et al. 1997). Contours start a 1.2×10^{-17} erg s^{-1} cm^{-2} arcsec^{-2} (about $\sim 1\sigma$ the detection limit), with a separation between consecutive contours of 6×10^{-17} erg s^{-1} cm^{-2} arcsec^{-2}. *Top-central panel*: narrow-band image of CIV. Contours start a 0.6×10^{-17} erg s^{-1} cm^{-2} arcsec^{-2}, which a separation between consecutive contours of 0.6×10^{-17} erg s^{-1} cm^{-2} arcsec^{-2}. *Top-right panel*: narrow-band image of HeII, with similar contour levels. *Bottom-left panel*: narrow-band image of Lyα extracted from the interpolated IFS datacube of the radio galaxy 4C 48.48, together with a grayscale image of the radio map radio map at 5 GHz, obtained at the VLA with A configuration (Carilli et al. 1997). Contours start a 1.2×10^{-17} erg s^{-1} cm^{-2} arcsec^{-2}, with a separation between consecutive contours of 6×10^{-17} erg s^{-1} cm^{-2} arcsec^{-2}. *Bottom-central panel*: narrow-band image of CIV. Contours start a 0.6×10^{-17} erg s^{-1} cm^{-2} arcsec^{-2}, with a separation between consecutive contours of 1.2×10^{-17} erg s^{-1} cm^{-2} arcsec^{-2}. *Bottom-right panel*: narrow-band image of HeII. Contours start a 0.6×10^{-17} erg s^{-1} cm^{-2} arcsec^{-2}, with a separation between consecutive contours of 3.5×10^{-17} erg s^{-1} cm^{-2} arcsec^{-2}. In all the panels the red solid circle indicates the original size of the PPAK fibres.

of the Lyα emission image to the coordinates of the peak emission of the Chambers et al. (1996) *U*-band image. For 4C 48.48 Chambers et al. (1996) published a registered Lyα narrow-band image of ~ 60 Å bandpass. The Lyα emission shows a well defined peak in this image. We used the coordinates of this peak to register our Lyα image. After registerin the Lyα images the rest of the narrow-band images and IFS data were registered using this astrometric solution. Taking into account the original size of the PPAK fibres, and the errors in the astrometry of the Chambers et al. (1996) images, we expect an accuracy not worse than $\sim 0.5''$ in the image registration.

We perform an independent check of the spatial registration performed. The coordinates of the field stars within the field-of-view of the IFS data, derived from the broad-band continuum image described before, where compared with those coordinates derived from the corresponding Digitized Sky Survey (DSS) POSS2 blue-band images. We found 5 stars in the field-of-view of the 4C 40.36 IFS data and 9 more in the field-of-view of the 4C 48.48 one. The coordinates of these stars match within a standard deviation of $\sim 0.3''$, which we consider the typical uncertainty of our spatial registration.

Once registered, the line emission maps can be compared with the emission in other wavelength ranges. Figure 2 shows, for each object, a counter-plot of the Lyα, CIV and HeII emission map, together with a radio map at 5 GHz, obtained at the VLA with the A configuration (Carilli et al. 1997). The remaining emission lines were not included in this comparison because they were not detected (NV in the case of 4C 48.48) or not detected as spatially extended (CIII] for both objects, and NV in the case of 4C 40.36). Note that the displayed images have been spatially interpolated to a regular grid using E3D, with a final sampling of $1''$/pix.

3.2. Velocity, FWHM and line ratio maps

Since it is the brightest and most extended of the emission lines within the spectral range of our data, we used Lyα as a means to extract information on the kinematics of the warm ionized gas associated with the two HzRGs. In each fibre where we detect Lyα, the line was fitted with a single Gaussian function, plus a low order polynomial function to describe the continuum, using FIT3D (Sánchez et al. 2007). The central wavelength, the
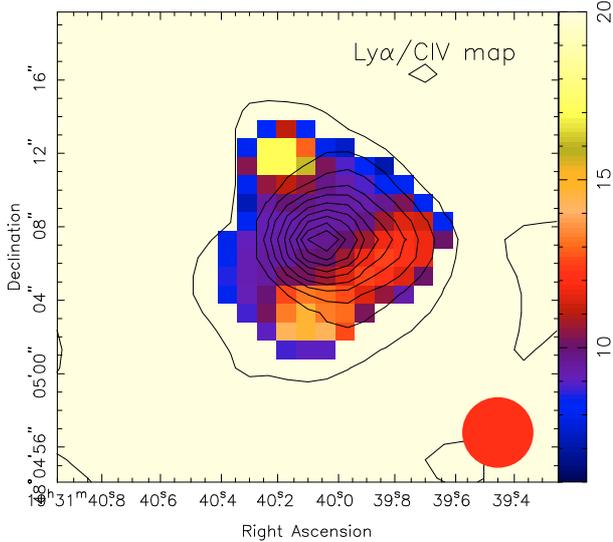
Fig. 3. Colour coded image of the spatial distribution of the Lyα/CIV emission line ratio for 4C 48.48, together with a contour plot of the Lyα emission line intensity, similar to the one shown in the corresponding panel of Fig. 4. Only where Lyα and CIV are both detected do we plot the ratios. The solid red circle indicates the size of the PPAK fibres, prior to resampling the data.

FWHM, and the integrated intensity were free parameters in the fitting process. The V300 and V600 datasets were analysed separately due to their different spectral resolutions. All values of velocity dispersion were corrected for the instrumental profile as listed in Table 1. The results were then spatially interpolated using E3D to create regular gridded images, with a final sampling of 1″/pix.

For both the velocity and velocity dispersion maps, we adopt the values at the position of the Lyα flux peak as our fiducial zero point. As a final step, we co-averaged the V300 and V600 datasets for each of the two HzRGs. (We note that for each of the two objects, the V300 and V600 datasets are very similar.) The velocity and *FWHM* maps for 4C+40.36 and 4C+48.48 are shown in Fig. 4.

In the case of 4C+48.48, we produced Lyα/CIV line ratio maps by simply dividing the interpolated Lyα map by those of CIV, respectively. This ratio map is shown in Fig. 3. Other line ratios, such as Lyα/HeII, CIV/HeII or CIV/CIII], have a lower signal to noise ratio in the spatially extended regions or are strongly affected by inaccuracies in the continuum subtraction, and hence they are not shown. In the case of 4C+40.36, the line ratio maps were rather noisy, and thus also are not shown here.

4. Results and discussion

4.1. The nuclear spectrum

Table 2 shows the results from fitting the emission lines in the fibre in which the line emission is brightest, which we assume includes the nucleus of the galaxy. The kinematic properties derived from the emission in this fibre are generally consistent with those reported by Villar-Martín et al. (2003). Table 3 shows emission line ratios composed from the Lyα, NV, CIV, HeII and CIII] lines in this fibre. For comparison, we also show the line ratios measured from Keck II long-slit spectra (Vernet et al. 2001; Humphrey 2005), for which the slit was aligned with the radio axis. Vernet et al. (2001) used relatively large extraction apertures of 4.7″ × 1.0″ and 6.2″ × 1.0″ for 4C+40.36

and 4C+48.48, respectively. Humphrey (2005), analysing the same spectra as Vernet et al. (2001), used extraction apertures of 2.1″ × 1.0″ for both objects.

From Table 3, it can be seen that several of the line ratios differ significantly between the different apertures. In the case of 4C+40.36, the NV/HeII ratio in our central fibre (and in the 2.5″ × 1.0″ aperture of Humphrey 2005) is almost twice that measured in the larger aperture of Vernet et al. (2001). For 4C+48.48, the NV/HeII, CIV/HeII, CIV/CIII] and CIII]/HeII ratios are ~1.5−2.4 times lower in our central fibre (and also in the 2.5″ × 1.0″ aperture of Humphrey 2005) than in the relatively large aperture of Vernet et al. (2001). Comparing these differences against ionization models (e.g. Humphrey et al. 2008), we consider that the two most plausible explanations are (a) a spatial gradient in gas metallicity, with higher metallicities closer to the nucleus for 4C+40.36, or with the oposite trend for 4C+48.48 (e.g. Overzier et al. 2001) or (b) a spatial gradient in the excitation level of the gas (e.g. Humphrey et al. 2007b), with higher excitation nearer the nucleus. More emission lines, such as NIV] 1749 or the forbidden optical lines, would be needed to break the degeneracy between these two possibilities (e.g. Humphrey et al. 2008). We can, however, conclude that within the extended nebulosities of both 4C+40.36 and 4C+48.48 the ionized gas has a significant range of physical conditions, as has been found for other HzRGs (e.g. Humphrey et al. 2007b).

4.2. Emission line morphologies

The Lyα emission from 4C+40.36 has a large spatial extent, and is distributed across ~12″ × 10″ (~100 kpc × 83 kpc: see Fig. 2). The CIV and HeII lines from this object are also spatially extended, and are aligned with the axis of the radio emission. As noted by previous investigators (e.g. Chambers et al. 1996b; Villar-Martín et al. 2003), the Lyα, CIV and HeII emission extends far beyond the radio structure. Their derivation of the spatial extention of these emission lines was limited by the position and aperture of the slit in their observations. Allowing for the low spatial resolution of our data, the distributions of the lines are broadly consistent with being within a pair of diametrically opposed "ionization cones" with an opening angle of ~90°, aligned with the radio axis. We have not obtained any clear detection of line emission in those regions that are outside any plausible ionization cone. From the spatially very extended Lyα emitting regions to the east (A in Fig. 2) and south-east (B) of the nucleus, we detect CIV and HeII, respectively. This shows that the gas in these regions is ionized, and is not merely a neutral Lyα "mirror" (e.g. Villar-Martín et al. 1996). The most distant knot of Lyα emission to the south-east of 4C+40.36 (C: at a radius of ~70 kpc) is also detected in broad band images (Chambers et al. 1996b), and thus may be associated with a companion galaxy.

Interestingly, the HeII line is brighter on the western side of 4C+40.36 than on the estern side, while the reverse is true for the CIV line. This might be due to a difference in the ionization properties or chemical abundances between the western and eastern emission line regions. However, we are unable to discriminate between these two possible explanations, because the CIV/HeII ratio is sensitive both to the ionization properties and the chemical abundance of the ionized gas (e.g. Vernet et al. 2001).

In the case of 4C+48.48, the Lyα emission is also very spatially extended, and is detected across ~14″ × 16″ (~116 kpc × 133 kpc). Its spatial extent parallel to the axis of
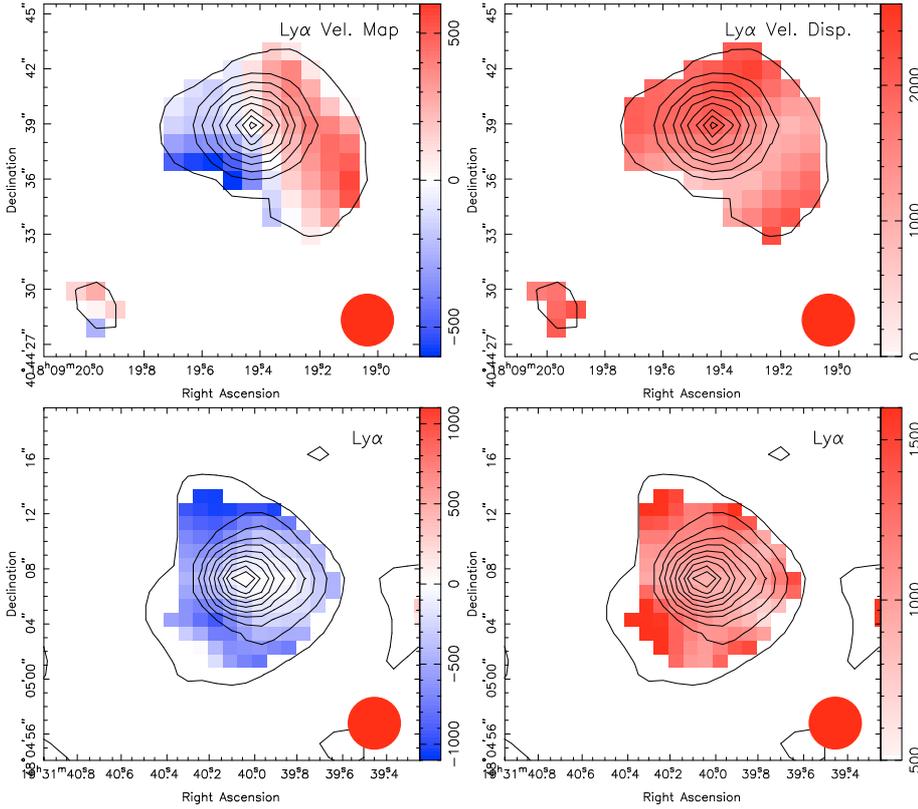
Fig. 4. *Top-left*: colour-coded image of the Lyα velocity map of 4C 40.36 together with a contour plot of the emission line intensity recovered by the fitting procedure. Contours start a 1.2×10^{-17} erg s^{-1} cm^{-2} arcsec^{-2}, which a separation between consecutive contours of 6×10^{-17} erg s^{-1} cm^{-2} arcsec^{-2}. Only the velocities corresponding to emission line fluxes above 1.2×10^{-17} erg s^{-1} cm^{-2} arcsec^{-2} are plotted. *Top-right*: similar plot for the Lyα velocity dispersion map derived by the fitting procedure. *Bottom-left*: similar plot to that of *top-left panel*, but for 4C 48.48. *Bottom-right*: similar plot to that of *top-right panel*, but for 4C 48.48. In all the panels the red solid circle indicates the original size of the PPAK fibres.

Table 2. Results of the fitting procedure for the peak emission spectra.

Object	Grating	Line Id. *	Wavelength (Å)	Flux **	*FWHM* (Å)***	*FWHM* km s^{-1}
4C 40.36	V300	Lyα	3961.03	45.83 ± 0.23	28.8	2179.7 ± 557.3
		NV	4043.84	2.45 ± 0.23	28.8	2135.1 ± 545.9
		CIV	5052.75	6.58 ± 0.20	35.6	2112.2 ± 540.1
		HeII	5352.34	3.60 ± 0.20	35.6	1994.0 ± 510.0
		CIII]λ1909	6222.77	3.46 ± 0.20	16.0	770.8 ± 196.9
	V600	Lyα	3967.39	62.11 ± 0.85	27.0	2040.2 ± 228.3
		NV	4050.35	2.67 ± 0.85	27.0	1998.4 ± 223.6
		CIV	5056.13	9.45 ± 0.33	21.4	1268.9 ± 142.0
4C 48.48	V300	Lyα	4057.26	46.66 ± 0.51	14.0	1034.5 ± 274.9
		Lyα 1	4058.39	37.47 ± 0.42	18.4	1359.2 ± 361.1
		Lyα 2	4055.83	11.36 ± 0.28	3.9	288.2 ± 76.6
		CIV	5170.31	5.16 ± 0.12	15.6	904.5 ± 240.3
		CIV 1	5172.25	4.13 ± 0.11	15.0	869.4 ± 231.0
		CIV 2	5165.23	1.00 ± 0.08	3.5	203.1 ± 54.0
		HeII	5474.06	4.89 ± 0.21	10.6	580.5 ± 154.2
		CIII]λ1909	6366.45	4.92 ± 0.19	17.9	842.9 ± 224.0
4C 48.48	V600	Lyα	4060.72	104.29 ± 1.21	13.0	959.7 ± 43.2
		Lyα 1	4063.55	51.31 ± 0.99	16.0	1180.4 ± 53.2
		Lyα 2	4059.41	52.60 ± 0.78	9.5	701.6 ± 31.6
		CIV	5172.39	9.30 ± 0.23	16.5	956.3 ± 43.1
		CIV 1	5175.85	6.16 ± 0.21	16.5	955.7 ± 43.1
		CIV 2	5168.53	3.17 ± 0.16	8.9	516.2 ± 23.3

(*) 1 indicate the broader components and 2 the narrower one; (**) 10^{-16} erg s^{-1} cm^{-2} arcsec^{-2}; (***) after removing the instrumental profile width.

the radio source is similar to the extent measured from the slit spectrum of Villar-Martín et al. (2003).

The Lyα, CIV and HeII emission lines from 4C+48.48 show a striking morphology. They extend several arcseconds towards the north-east, in close alignment with the radio source. However, on the other side of the nucleus, this alignment with the radio source is not present: while the south-western radio

source undergoes a dramatic ~45 deg bend to the south, the line emission extends ~5″ (~40 kpc) from the nucleus towards the west. In this object, we note that the CIV and HeII lines have very similar spatial distributions to that of Lyα. This shows that the giant nebula is ionized. Moreover, the presence of HeII emission rules out ionization by young stars, but is consistent with photoionization by the obscured AGN (e.g. Vernet et al. 2001).

Table 3. Line ratios for the total emission and the perturbed and quiescent components with it was possible to decouple them.

Object	Dataset	Lyα/HeII	Lyα/CIV	Lyα/NV	NV/HeII	CIV/HeII	CIV/CIII]	CIII]/HeII
4C 40.36	V300	12.73 ± 0.23	6.97 ± 0.07	18.71 ± 0.48	0.68 ± 0.03	1.83 ± 0.05	1.90 ± 0.05	0.96 ± 0.03
	V600		6.57 ± 0.13	23.26 ± 1.45				
	V01*	14.7	8.4	39.2	0.37	1.8	1.8	1.0
	H05**	11.6	7.1	19.3	0.6	1.6	2.2	0.7
4C48.48	V300	9.57 ± 0.13	9.04 ± 0.12	>17.9	<0.38	1.06 ± 0.03	1.05 ± 0.03	1.01 ± 0.03
	Broader		9.07 ± 0.15					
	Narrower		11.36 ± 0.75					
4C48.48	V600		11.21 ± 0.21	>65.2				
	Broader		8.33 ± 0.24					
	Narrower		16.59 ± 0.88					
	V01*	13.2	12.6	48.3	0.27	1.0	1.7	0.6
	H07**	11.3	8.2	12.6	0.9	1.4	2.6	0.5

* Vernet et al. (2001); ** Humphrey (2005).

We note here that the two-dimesional extensions of the CIV and HeII emission lines have been reported for the first time in the current study.

4.3. Lyα/CIV map of 4C+48.48

Figure 3 shows the spatial distribution of the Lyα/CIV line ratio. Since the HeII image is affected by the presence of the nearby field star, we do not show a Lyα/HeII map. Previous investigations using long-slit spectroscopy (Humphrey et al. 2007a) revealed that line ratios involving Lyα vary significantly *along the radio axis*. Our Lyα/CIV map confirms their result and, moreover, shows that this ratio also varies substantially in two spatial dimensions.

The line ratio map reveals a band of relatively low Lyα/CIV, running perpendicular to the radio axis, and passing through the position of maximum Lyα flux. In this band, we measure Lyα/CIV ratios as low as 8, whereas standard photoionization models predict Lyα/CIV $\gtrsim$ 10 (e.g. Villar-Martín et al. 2007a). Thus, we consider these relatively low observed values of Lyα/CIV to be the result of absorption of Lyα, presumably by neutral hydrogen or interstellar dust. We suggest that this band of Lyα absorption might be the observational signature of an edge-on disc of gas and dust associated with the radio galaxy host (e.g. Gopal-Krishna & Wiita 2000).

To the south-west and north-east of the low Lyα/CIV band, we measure Lyα/CIV ratios of ~11−15, which are consistent with the values predicted by standard photoionization models (e.g. Villar-Martín et al. 2007a).

4.4. Emission line kinematics

Figure 4 (top-left panel) shows a colour coded image of the Lyα velocity map for 4C+40.36, together with a contour plot of the intensity of this line. Since we do not detect any stellar absorption lines from which to determine the systemic velocity, we have simply adopted the velocity at the position of the Lyα emission peak as our fiducial zero point. It is important to recognise that this velocity may not necessarily correspond to the true systemic velicity, as discussed by Humphrey et al. (2008)

This velocity map shows a somewhat regular pattern, with a clear gradient from east to west. The maximum velocity amplitude is ~1000 km s^{-1}, with the gas to the east approaching and the gas to the west receding, relative to the fiducial velocity zero-point. This is consistent with the velocity curves obtained by Villar-Martín et al. (2003) using a 1″ slit along the radio axis.

The region of null velocity runs from north-east to south-west, i.e., at an angle of ~45° relative to the axis of the radio and line emission (see Fig. 3).

The relatively ordered nature of the velocity map suggests that the kinematics of the ionized gas are dominated by ordered motion, i.e., infall, outflow or rotation. Superficially, the map is consistent with each of these three possibilities, and we are unable to definitively distinguish between them. However, we argue that since the *FWHM* and velocity amplitude are both roughly twice what one would expect for gravitational motion around a giant elliptical galaxy (e.g. Villar-Martín et al. 2002), at least part of the Lyα nebula associated with 4C+40.36 has been kinematically perturbed, presumably by the radio source, as suggested by Villar-Martín et al. (2003). Moreover, we note that the average *FWHM* would seem rather large relative to the velocity amplitude ($\sigma/v \sim 1$) for a stable rotating system, even without correcting for inclination. In addition, we do not observe the broadening of the *FWHM* at the null velocity that would be expected in the case of rotation.

The lower left panel of Fig. 4 shows the colour-coded representation of the Lyα velocity map of 4C+48.48. As before, we define our fiducial zero as the velocity at the peak of the Lyα emission. The *FWHM* shows little spatial variation, with a typical value of 1000 km s^{-1}, and with slightly higher values in the outer regions. As we also noted for 4C+40.36, we find that the kinematics of 4C+48.48 are inconsistent with stable rotation: the *FWHM* is rather high compared to the amplitude of the velocity shifts, and there is no clear broadening of the *FWHM* near the galaxy nucleus or the null velocity. Taken at face value, this velocity map is consistent with either infall or outflow.

5. Summary

In this paper we have presented integral field spectroscopic data-cubes for two HzRGs, namely 4C+40.36 and 4C+48.48; this study is part of a wider programme in which we use this technique (Villar-Martín et al. 2006, 2007b) to obtain information relating to the nature of the spatially extended gas associated with HzRGs, and their possible connection with the nuclear and radio-jet acivity.

Although both objects have been observed before using slit-spectroscopy, in the same wavelength range, we present for the first time IFS data on them. This techinique allows us to study the spatial distribution of the emission in the direction perpendicular to the radio-jet axis, that in many cases is not covered by long-slit spectroscopy.

For both sources, the Lyα emission is extended across 100 kpc or more, in agreement with previous imaging and spectroscopic studies (Chambers et al. 1996b; Villar-Martín et al. 2003). The CIV and HeII emission lines are also spatially extended. While these emission lines are generally aligned with the axis of the radio emission, we also detect emission far from this axis.

Our map of the Lyα/CIV ratio in 4C+48.48 has revealed a band of low Lyα/CIV running perpendicular to the radio axis, through the assumed position of the active nucleus. We suggest that this feature might be the observational signature of an edge-on disc of neutral gas (e.g. Gopal-Krishna & Wiita 2000).

We have argued that when viewed in two spatial dimensions, the kinematic properties of both 4C+40.36 and 4C+48.48 are inconsistent with stable rotation. However, their properties are not inconsistent with infall (e.g. Humphrey et al. 2007a) or outflows (Nesvadba et al. 2006).

References

Baum, S. A., Heckman, T., & van Breugel, W. 1990, ApJS, 74, 389

Best, P. N. 2007, New Astron. Rev., 51, 168

Carilli, C. L., Roettgering, H. J. A., van Ojik, R., Miley, G. K., & van Breugel, W. J. M. 1997, ApJS, 109, 1

Carson, J. E., Larkin, J. E., McLean, I. S., et al. 2001, ApJ, 563, 63

Chambers, K. C., Miley, G. K., van Breugel, W. J. M., et al. 1996, ApJS, 106, 247

Christensen, L., Jahnke, K., Wisotzki, L., & Sánchez, S. F. 2006, A&A, 459, 717

Di Matteo, T., Springel, V., & Hernquist, L. 2005, Nature, 433, 604

Eales, S. A., Rawlings, S., Dickinson, M., et al. 1993, ApJ, 409, 578

Egami, E., Armus, L., Neugebauer, G., et al. 2003, AJ, 125, 1038

García-Lorenzo, B., Sánchez, S. F., Mediavilla, E., González-Serrano, J. I., & Christensen, L. 2005, ApJ, 621, 146

Humphrey, A. 2005, Ph.D. Thesis

Humphrey, A., Villar-Martín, M., Fosbury, R., Vernet, J., & di Serego Alighieri, S. 2006, MNRAS, 369, 1103

Humphrey, A., Villar-Martín, M., Fosbury, R., et al. 2007a, MNRAS, 375, 705

Humphrey, A., Iwamuro, F., Villar-Martín, M., et al. 2007b, MNRAS, 382, 1729

Humphrey, A., Villar-Martín, M., Vernet, J., et al. 2008, MNRAS, 383, 11

Husemann, B., Wisotzki, L., Sánchez, S. F., & Jahnke, K. 2008, A&A, 488, 145

Kang, X., van den Bosch, F. C., & Pasquali, A. 2007 [arXiv:0704.0932]

Kelz, A., Verheijen, M. A. W., Roth, M. M., et al. 2006, PASP, 118, 129

Kurk, J. D., Pentericci, L., Röttgering, H. J. A., & Miley, G. K. 2002, Rev. Mex. Astron. Astrofis. Conf. Ser., 13, 191

Maxfield, L., Spinrad, H., Stern, D., Dey, A., & Dickinson, M. 2002, AJ, 123, 2321

McCarthy, P. J. 1993, ARA&A, 31, 639

McCarthy, P. J., Spinrad, H., Dickinson, M., et al. 1990, ApJ, 365, 487

McCarthy, P. J., Spinrad, H., & van Breugel, W. 1995, ApJS, 99, 27

Reuland, M., van Breugel, W., Röttgering, H., et al. 2003, ApJ, 592, 755

Roth, M. M., Kelz, A., Fechner, T., et al. 2005, PASP, 117, 620

Sánchez, S. F. 2004, AN, 325, 167

Sánchez, S. F. 2006, AN, 327, 850

Sánchez, S. F., García-Lorenzo, B., & Pecontal-Rousset, A. 2007, Proceedings of the XIII IAC Winter School, ed. S. Arribas, E. Mediavilla, & M. Roth, in press

Tadhunter, C. N., Fosbury, R. A. E., & Quinn, P. J. 1989, MNRAS, 240, 225

Tody, D. 1993, IRAF in the Nineties in Astronomical Data Analysis Software and Systems II, ed. R. J. Hanisch, R. J. V. Brissenden, & J. Barnes, ASP Conf. Ser., 52, 173

van Ojik, R., Roettgering, H. J. A., Miley, G. K., & Hunstead, R. W. 1997, A&A, 317, 358

Veilleux, S., Cecil, G., & Bland-Hawthorn, J. 2005, ARA&A, 43, 769

Verheijen, M. A. W., Bershady, M. A., Andersen, D. R., et al. 2004, AN, 325, 151

Vernet, J., Fosbury, R. A. E., Villar-Martín, M., et al. 2001, A&A, 366, 7

Villar-Martín, M., Alonso-Herrero, A., di Serego Alighieri, S., & Vernet, J. 2000, A&AS, 147, 291

Villar-Martín, M., Vernet, J., di Serego Alighieri, S., et al. 2003, MNRAS, 346, 273

Villar-Martín, M., Sánchez, S. F., De Breuck, C., et al. 2006, MNRAS, 366, L1

Villar-Martín, M., Humphrey, A., De Breuck, C., et al. 2007a, MNRAS, 375, 1299

Villar-Martín, M., Sánchez, S. F., Humphrey, A., et al. 2007b, MNRAS, 378, 416